

S. Tanaka · H. Suzuki · S. Ueda · S. Sannomaru

# An extended wavelet Galerkin method with a high-order B-spline for 2D crack problems

Received: date / Accepted: date

**Abstract** Two-dimensional (2D) crack problems are solved employing a novel technique based on a combination of wavelet Galerkin method (WGM) and X-FEM with a high-order interpolant. Multiresolution analysis of the wavelet basis functions (scaling/wavelet functions) plays an important role in the numerical simulation. High-order B-spline scaling/wavelet functions are chosen as the basis functions. Severe stress concentration near a crack tip is represented by superposing the multiresolution wavelet functions. In addition, the crack modeling is easy to treat by introducing enrichment functions of the X-FEM. In the proposed approach, the governing equation is discretized based on fixed-grid, fracture mechanics problems with complicated shaped geometries can be analyzed effectively, reducing the model generation tasks. 2D linear fracture mechanics problems are solved and the accuracy is studied for numerical examples.

**Keywords** Wavelet Galerkin method · X-FEM · High-order B-splines · Fracture mechanics analysis

## 1 Introduction

The wavelet method is widely applied in signal processing, data compression, computer graphics, and image denoising. Multiresolution analysis (MRA) is one of the attractive features of wavelet theory. It is easy to control the spatial and time resolution in wavelet analysis employing MRA. A signal or function can be decomposed into different resolution levels with hierarchical wavelet bases. A basic concept and mathematical representations of the wavelet method are presented in [1–3]. Applications of the wavelet method to analyze partial differential equations have been studied [4–6]. Researchers have developed new methods, such as the wavelet collocation method [7], wavelet Galerkin method (WGM) [8, 9], wavelet-based finite element method (wavelet FEM) [10, 11], and wavelet-based boundary element method (wavelet BEM) [12, 13], to solve physical, science and engineering problems. Other wavelet-based methods and related research are summarized in [14]. The present study focuses on the WGM

---

S. Tanaka  
Graduate School of Engineering, Hiroshima University, Kagamiyama 1-4-1, Higashi-Hiroshima, Hiroshima, 739-8527, Japan  
Tel.: +81-82-424-7859  
Fax: +81-82-422-7194  
E-mail: satoyuki@hiroshima-u.ac.jp

H. Suzuki  
E-mail: m140825@hiroshima-u.ac.jp

S. Ueda  
E-mail: m132821@hiroshima-u.ac.jp

S. Sannomaru  
E-mail: d126490@hiroshima-u.ac.jp

---

to analyze fracture mechanics problems.

When solving solid and structural problems employing the WGM, the body is placed on a fixed-grid and divided by equally spaced structured cells. The stiffness matrix is numerically integrated using the structured cells. Such modeling is sometime called a fixed-grid (voxel-based) approach [15,16]. Wavelet basis functions (scaling/wavelet functions) are employed as the basis functions in the WGM. They are periodically located on the analysis model to approximate deformations. The solution at the lowest-resolution level is approximated by scaling functions, and the solutions at the higher-resolution levels are approximated by multilevel wavelet functions. In addition, the spatial resolution of the wavelet Galerkin (WG) analysis can easily be controlled employing MRA. The wavelet functions are superposed locally where high spatial resolution is needed. Therefore, the WGM can be considered an enhanced voxel approach, and high-accuracy computation is carried out with fewer degrees of freedom (DOFs) employing the fixed-grid discretization. The WGM has been applied to solve solid and structural problems. Diaz [9] solved large-scale boundary value problems on simple domains. Nakagoshi and Noguchi [17], and Zhang *et al.* [18] analyzed plate bending problems. One-dimensional (1D) elastic-plastic problems were analyzed in [19,20]. Jang *et al.* [21] developed an adaptive WGM for 2D elliptic problems using a fictitious domain approach. In addition, topology optimization problems were solved in [22–24]. Because most of the WGMs were discretized based on the fixed-grid, boundary value problems with complicated shaped boundaries were easy to treat.

The MRA in the WGM is attractive for solving fracture mechanics problems. The severe stress concentration near the crack tip is represented employing hierarchical wavelet bases. The author's previous study [25] analyzed solid mechanics problems employing the WGM with B-spline scaling/wavelet functions [26]. However, there are difficulties in treating displacement jumps across the crack surface because the displacements are assumed continuous across the entire analysis domain. Enrichment functions of the extended finite element method (X-FEM) [27,28] were introduced in the WGM to solve 2D crack problems and simulate crack propagation [29]. The Heaviside function was enriched to a linear B-spline scaling function to allow the displacement discontinuity of the crack surface. Additionally, asymptotic fields near the crack tip were enriched to linear B-spline scaling/wavelet functions to represent the crack tip geometry, and to improve the solution around the crack tip. Li and Ghosh [30,31] solved multiple crack propagation problems employing the wavelet method and extended Voronoi cell FEM. The solution near the crack tip was improved employing multiresolution wavelet functions. Additionally, dynamic fracture problems were solved using enriched meshfree method [32] and XFEM/spectral element method [33]. Accuracy in the crack analyses are improved employing a high-order interpolant.

In the present study, 2D crack problems are solved by the combination of the WGM and X-FEM with a high-order function. Quadratic and cubic cardinal B-splines are employed to construct the wavelet bases in the WGM. When introducing the enrichment functions to the high-order B-splines, continuous stress/strain fields are obtained in representing severe stress concentration near the crack tip. In addition, complex shaped geometries are easy to treat based on the fixed-grids, and the spatial resolution of the analysis model is easy to control. Although wavelet basis functions were introduced in X-FEM in our previous study [29], the linear B-spline scaling/wavelet functions were only employed. The function supports of the high-order B-spline wavelet bases are wider than those of the linear B-spline case, and a number of the basis functions overlap each other. We examine the introduction of the enrichment functions to the high-order B-spline wavelet bases. A highly accurate fracture mechanics analysis will be carried out with fewer DOFs employing the present method. Accuracy in SIFs is examined employing the linear, quadratic and cubic B-splines, and the effectiveness of the proposed approach is demonstrated using several fracture mechanics problems with curved boundaries.

This paper is organized as follows. Chapter 2 briefly introduces multiresolution wavelet basis functions with a cardinal B-spline. Chapter 3 presents the analysis for 2D crack problems employing the WGM with high-order B-spline functions and evaluates the stress intensity factors (SIFs) in the WG analysis. Chapter 4 solves 2D linear fracture mechanics problems, and the accuracy is examined. Chapter 5 presents concluding remarks.

## 2 Wavelet method

### 2.1 B-spline scaling/wavelet functions

So far, several scaling/wavelet functions have been adopted as wavelet basis functions for solving partial differential equations; *e.g.*, Daubechies wavelets [5, 7], affine fractal wavelets [11], the hierarchical Schauder basis [34], spline-based wavelets [10, 12, 22], hat interpolation wavelets [21, 24] and Gaussian wavelets [30, 31]. The present study adopts cardinal spline wavelets proposed by Chui and Wang [26]. Here, the basic concept of the cardinal B-splines, and the mathematical representation of the scaling/wavelet functions are briefly described.

The B-spline scaling functions can be written with truncated power series as

$$\begin{aligned} \phi_i^\mu(x) &= \frac{1}{(\mu-1)!} \sum_{k=0}^{\mu} (-1)^k {}_{\mu}C_k (x-k)_+^{\mu-1}, \\ x_+ &= \max\{0, x\}, \\ x_+^\mu &= (x_+)^{\mu}, \end{aligned} \quad (1)$$

where  $\phi_i^\mu(x)$  is the  $\mu$ -th-order B-spline scaling function. The B-spline scaling/wavelet functions have two-scale relations [26]. The two-scale sequence  $p_k^\mu$  of the  $(\mu-1)$ -th-order B-spline scaling functions can be written as

$$p_k^\mu = \frac{1}{2^{\mu-1}} {}_{\mu}C_k, \quad (k = 0, \dots, \mu). \quad (2)$$

Alternatively, the B-spline wavelet functions  $\psi_i^\mu(x)$  can be constructed employing the two-scale relation as the sequences

$$q_k^\mu = \frac{(-1)^k}{2^{\mu-1}} \sum_{i=0}^{\mu} {}_{\mu}C_i \phi_i^{2\mu}(k+1-i), \quad (k = 0, \dots, 3\mu-2), \quad (3)$$

where  $q_k^\mu$  denote two-scale sequences of the wavelet functions. This research adopts quadratic ( $\mu = 3$ ) and cubic ( $\mu = 4$ ) B-spline scaling/wavelet functions. 1D wavelet bases are schematically illustrated in Figs.1 (a) and (b). For example, two-scale relations of the quadratic B-spline scaling/wavelet functions are schematically illustrated in Figs.2 (a) and (b). They are represented by the linear combinations of one-step higher-resolution scaling functions. In addition, the 2D B-spline wavelet bases are obtained from tensor products of the 1D wavelet bases. The function shapes of the 2D quadratic B-spline scaling/wavelet functions  $\Phi^3(\mathbf{x})(= \phi^3(x_1)\phi^3(x_2))$ ,  $\Psi^{3,1}(\mathbf{x})(= \phi^3(x_1)\psi^3(x_2))$ ,  $\Psi^{3,2}(\mathbf{x})(= \psi^3(x_1)\phi^3(x_2))$  and  $\Psi^{3,3}(\mathbf{x})(= \psi^3(x_1)\psi^3(x_2))$  are presented in Figs.3 (a)-(d).

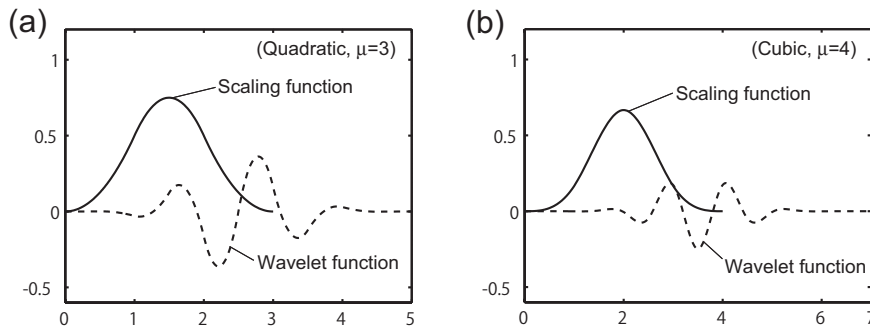


**Fig. 1** 1D high-order B-spline scaling/wavelet functions: **a** Quadratic B-spline ( $\mu = 3$ ), **b** Cubic B-spline ( $\mu = 4$ )

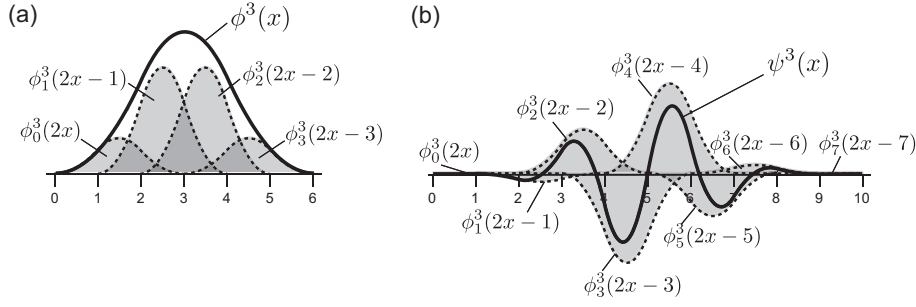


**Fig. 2** Schematic illustrations of two-scale relations (Quadratic B-spline): **a** Scaling function  $\phi^3(x)$ , **b** Wavelet function  $\psi^3(x)$

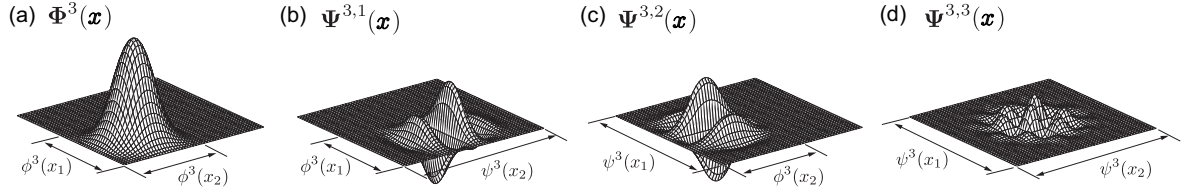


**Fig. 3** 2D quadratic B-spline wavelet bases: **a**  $\Phi^3(\mathbf{x})$ , **b**  $\Psi^{3,1}(\mathbf{x})$ , **c**  $\Psi^{3,2}(\mathbf{x})$ , **d**  $\Psi^{3,3}(\mathbf{x})$

## 2.2 MRA in the WGM with B-spline wavelet bases

The spatial resolution of the analysis model and the function supports of the wavelet bases are discussed in 1D case. For example, arrangements of the quadratic ( $\mu = 3$ ) B-spline scaling functions are shown in Fig.4 (a). Equally spaced nodes are distributed along the 1D space, and the scaling functions are located equidistantly. The level- $l$  model is approximated by the level- $l$  scaling functions  $\phi_{l,i}^3(2^l x - i)$  ( $=\phi_{l,i}^3(x)$ ). The level- $l$  scaling functions are located at each node  $(\dots, i-1, i, i+1, \dots)$  in the level- $l$  model. The level- $(l-1)/(l+1)$  models are the one-step lower/higher-resolution models of the level- $l$  model. The function supports and the node spacing of the level- $(l-1)/(l+1)$  scaling functions become  $2^{-1}/2$  times those of the level- $l$  scaling functions. Therefore, the spatial resolution of the analysis model can be controlled by changing the resolution level- $l$ .

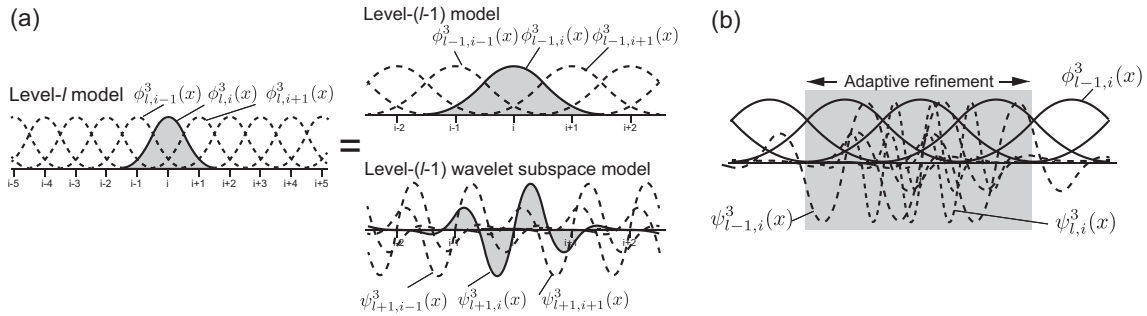


**Fig. 4** 1D arrangements of quadratic B-spline scaling/wavelet functions: **a** Definition of resolution level, **b** Adaptive refinement

In the WGM, the wavelet functions are superposed on the scaling functions to control the spatial resolution of the analysis model. The level- $l$  wavelet functions are defined as  $\psi_{l,i}^3(2^l x - i)$  ( $=\psi_{l,i}^3(x)$ ). The wavelet functions are also arranged equidistantly, and the function supports and the node spacing change in accordance with the resolution level- $l$ . Arrangements of the level- $(l-1)$  scaling/wavelet functions  $\phi_{l-1,i}^3(x) / \psi_{l-1,i}^3(x)$  are also shown in Fig.4 (a). The function space of the level- $(l-1)$  wavelet functions is called the level- $(l-1)$  wavelet subspace. Employing MRA, the level- $l$  model can

be generated by superposing the level- $(l-1)$  wavelet subspace onto the level- $(l-1)$  model. This is the so-called MRA in the WGM.

Furthermore, multilevel wavelet functions can be superposed locally on the lowest-resolution model to control the spatial resolution adaptively. The adaptive refinements in the level- $(l-1)$  model are schematically illustrated in Fig.4 (b). In this figure, the level- $(l-1)$  and  $-l$  wavelet functions  $\psi_{l-1,i}^3(x)$  and  $\psi_{l,i}^3(x)$  are partially superposed on the level- $(l-1)$  model. Highly accurate numerical simulations are carried out by changing the spatial resolution adaptively. In our previous study, MRA in the WGM was conducted using B-spline wavelet bases, and an adaptive strategy was developed to analyze 2D solid mechanics problems [25].

### 3 2D crack analysis employing the WGM

#### 3.1 Basis functions and structured cells

To analyze 2D fracture mechanics problems, high-order B-spline scaling/wavelet functions are adopted as the basis functions. In the proposed approach, a structured cell is employed to integrate the stiffness matrix. Here, relationships between the basis functions and the structured cells in the different resolution models are briefly discussed. Arrangements of the 1D quadratic and cubic B-spline scaling/wavelet functions are respectively represented in Figs.5 (a) and (b). The central coordinates (nodes) of the basis functions are also shown in the figures. Here, the lowest-resolution model is assumed to be the level- $l$  model, and level- $l$  scaling functions are periodically located in the model. A domain is divided by equally spaced level- $l$  cells. In addition, the level- $l$  and  $-(l+1)$  wavelet functions are superposed on the level- $l$  model to generate the level- $(l+1)$  and  $-(l+2)$  models. The width of the cells are half that for the level- $l \rightarrow -(l+1)$  models. These cells are called the level- $(l+1)$  and  $-(l+2)$  cells. Although the function supports and the positions of the quadratic and cubic B-splines are slightly different, the basis functions and the cells are generated in the analysis models consistently.

The concept of the 1D case can easily be extended to the 2D case. The nodes of the 2D quadratic and cubic B-spline scaling/wavelet functions are respectively presented in Figs.6 (a) and (b). The level- $l$  scaling functions are periodically located within a unit domain, and the model is assumed to be the level- $l$  model. The rectangular region between the level- $l$  scaling functions is called the level- $l$  cell. The level- $(l+1)$  and  $-(l+2)$  models can be generated by superposing the level- $l$  and  $-(l+1)$  wavelet functions. As the spatial resolution increases, the size of the cell becomes a quarter of the size of the original cell. These cells are called the level- $(l+1)$  and  $-(l+2)$  cells, respectively.

In fracture mechanics analysis, a discontinuous function is introduced to the scaling functions, and an asymptotic solution near the crack tip is introduced to the scaling/wavelet functions. A partition of unity (PU) condition [35] of the scaling/wavelet functions is examined for introducing the enrichment functions in the WGM. 1D level- $l$   $\mu$ -th-order B-spline scaling functions and level- $l$  and  $-(l+1)$  wavelet functions are employed. The PU condition of the 2D scaling/wavelet functions can be written as

$$\begin{aligned} \sum_{i,j \in \Omega} \Phi_{l,i,j}^{\mu}(\mathbf{x}) &= 1, \\ \sum_{i,j \in \Omega} \Psi_{l,i,j}^{\mu,m}(\mathbf{x}) &\neq 1 \quad (m = 1, \dots, 3), \\ \sum_{i,j \in \Omega} \Psi_{l+1,i,j}^{\mu,m}(\mathbf{x}) &\neq 1 \quad (m = 4, \dots, 8). \end{aligned} \quad (4)$$

Therefore, the scaling functions satisfy the PU condition, but the wavelet functions do not. Although the wavelet functions do not have PU, fracture mechanics problems can be analyzed [29]. Furthermore, the solutions will be improved because continuous stress/strain fields are obtained when employing the high-order B-spline wavelet bases. We carried out convergence studies and examined the accuracy in numerical examples.

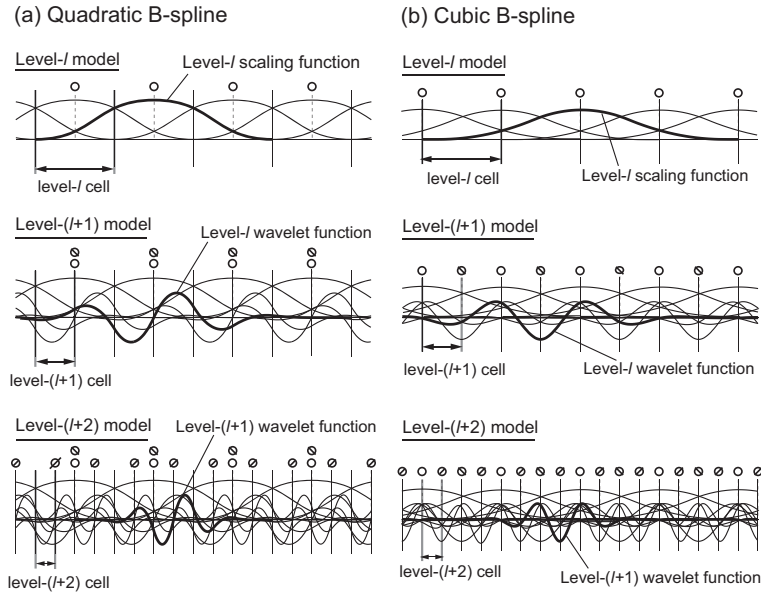


**Fig. 5** Arrangement of the 1D high-order B-spline scaling/wavelet functions: **a** Quadratic B-spline, **b** Cubic B-spline

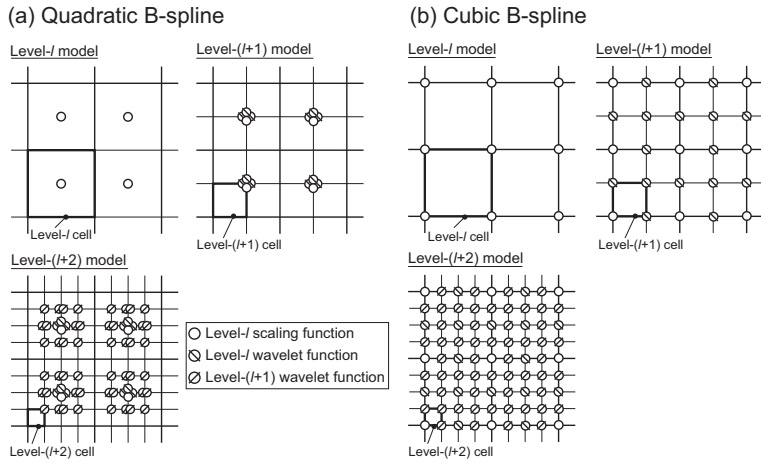


**Fig. 6** Arrangement of the 2D high-order B-spline scaling/wavelet functions **a** Quadratic B-spline, **b** Cubic B-spline

### 3.2 WGM for 2D fracture mechanics problems

A boundary value problem for 2D fracture mechanics problems is discussed. A cracked elastostatic body is presented in Fig.7 (a). There are two cracks. One is an edge crack and the other is an internal crack emanating from a hole. The analysis domain is  $\Omega$ , and the boundary is  $\Gamma$ . The boundary consists of the traction boundary  $\Gamma_t$ , the prescribed displacement boundary  $\Gamma_u$ , and the crack surface  $\Gamma_c$ .  $\mathbf{t}$  represents a traction force and  $\mathbf{u}$  is the prescribed displacement.  $\Omega_+$  and  $\Omega_-$  represent one side and the other side of the crack surface  $\Gamma_c$ . A traction-free condition is imposed on  $\Gamma_c$ .

WG discretization of the 2D crack problem employing the quadratic B-spline wavelet bases is schematically represented in Fig.7 (b). The deformation of the cracked body is approximated by the scaling/wavelet functions. The level- $l$  scaling functions are employed across the entire analysis domain. The nodes and the function supports are shown in Fig.7 (b). In addition, level- $l$ ,  $-(l+1)$ ,  $-(l+2)$ ,  $\dots$  wavelet functions and the enrichment functions are introduced to model the cracks. The analysis

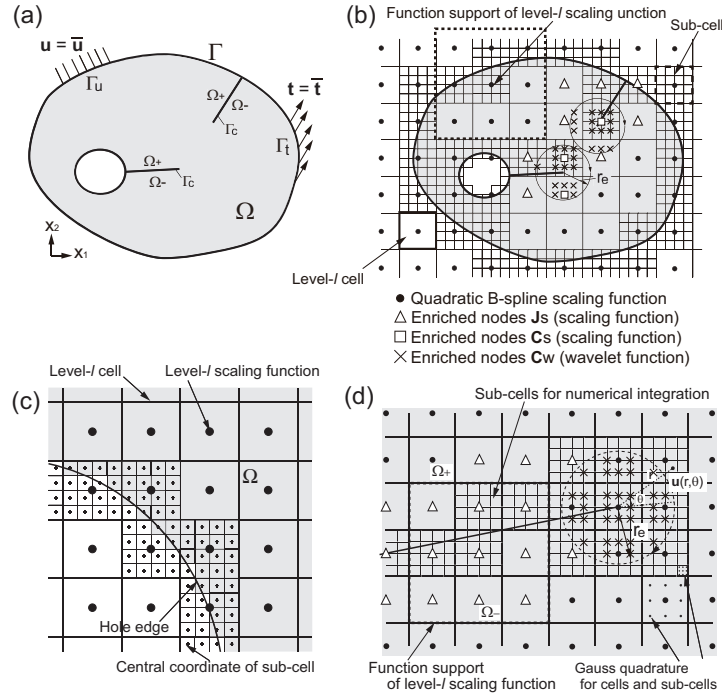


**Fig. 7** Boundary value problem to be solved: **a** Cracked elastostatic body, **b** WG discretization (Quadratic B-spline), **c** Modeling of the external boundary (Sub-cells for the boundary representation), **d** Modeling near the crack tip (Sub-cells for the numerical integration)

domain is divided by equally spaced structured cells (*i.e.*, level- $l$  cells) to integrate the stiffness matrix numerically. A close-up view of a external boundary of the body is schematically presented in Fig.7 (c). To accurately model the external boundaries and the hole edges, the level- $l$  cells are further divided by equally spaced sub-cells. When the central coordinates of the cells and the sub-cells are within the analysis domain, the stiffness matrix is numerically integrated.

The details of the crack modeling are presented in Fig.7 (d). To allow the presence of cracks in the WGM, the enrichment functions are introduced. To represent severe stress concentration around the crack tip, asymptotic solutions near crack tip are enriched to scaling/wavelet functions. In addition, the Heaviside step function is enriched to scaling functions that represent the displacement discontinuity of the crack face. The positions of the scaling/wavelet functions and the enrichment functions are illustrated in Figs.7 (b) and (d). The level- $(l+1)$  displacement  $\mathbf{u}_{l+1}^{xw}(\mathbf{x})$  of the extended WGM (XWGM) can be written as

$$\begin{aligned} \mathbf{u}_{l+1}^{xw}(\mathbf{x}) = & \sum_{i,j} \mathbf{a}_{l,i,j} \Phi_{l,i,j}^3(\mathbf{x}) + \sum_{m=1}^3 \sum_{i,j} \mathbf{b}_{l,i,j}^m \Psi_{l,i,j}^{3,m}(\mathbf{x}) + \sum_{i,j \in J_s} H(\mathbf{x}) \Phi_{l,i,j}^3(\mathbf{x}) \mathbf{c}_{l,i,j} \\ & + \sum_{i,j \in C_s} \Phi_{l,i,j}^3(\mathbf{x}) \sum_{n=1}^{n_e} \gamma_n(\mathbf{x}) \mathbf{d}_{l,i,j}^n + \sum_{m=1}^3 \sum_{i,j \in C_w} \Psi_{l,i,j}^{3,m}(\mathbf{x}) \sum_{n=1}^{n_e} \gamma_n(\mathbf{x}) \mathbf{e}_{l,i,j}^n \end{aligned} \quad (5)$$

where the first and second terms are the level- $l$  quadratic B-spline scaling functions  $\Phi_{l,i,j}^3(\mathbf{x})$  and the wavelet functions  $\Psi_{l,i,j}^{3,m}(\mathbf{x})$  ( $m=1, 2, 3$ ) that approximate the level- $(l+1)$  displacements in the standard WGM.  $\mathbf{a}_{l,i,j}$  and  $\mathbf{b}_{l,i,j}^m$  are coefficients of the scaling/wavelet functions. The third term is the enrichment term that represents the displacement discontinuity at the crack face.  $\mathbf{c}_{l,i,j}$  denotes the coefficients of the basis functions.  $H(\mathbf{x})$  is the Heaviside step function, written as

$$H(\mathbf{x}) = \begin{cases} 1, & (\mathbf{x} \text{ in } \Omega_+) \\ -1, & (\mathbf{x} \text{ in } \Omega_-). \end{cases} \quad (6)$$

The enrichment nodes in terms of the third term are denoted "nodes  $\mathbf{J}_s$ ". Each scaling function belonging to cells cut or partially cut by the crack segment includes nodes  $\mathbf{J}_s$ . The locations of the nodes  $\mathbf{J}_s$  are presented in Figs.7 (b) and (d). The fourth and fifth terms are enrichment terms that represent severe stress concentration near the crack tip for the scaling functions and the wavelet functions, respectively. Asymptotic fields near the crack tip in linear fracture mechanics are now introduced. The crack tip functions  $\gamma_n(\mathbf{x})(n = 1, \dots, n_e)$  can be written as

$$\gamma_1(\mathbf{x}) = \sqrt{r} \sin \frac{\theta}{2}, \quad \gamma_2(\mathbf{x}) = \sqrt{r} \cos \frac{\theta}{2}, \quad \gamma_3(\mathbf{x}) = \sqrt{r} \sin \frac{\theta}{2} \sin \theta, \quad \gamma_4(\mathbf{x}) = \sqrt{r} \cos \frac{\theta}{2} \sin \theta, \quad (7)$$

where  $(r, \theta)$  are the polar coordinates from the crack tip.  $n_e$  is the number of functions. When  $n_e=1$  is chosen, only  $\gamma_1(\mathbf{x})$  is adopted; when  $n_e=4$  is chosen, all functions are employed. The fourth and fifth terms are employed for the scaling/wavelet functions in the radius  $r_e$  from the crack tip. The nodes belonging the fourth and fifth terms are respectively assigned "nodes  $\mathbf{C}_s$ " and "nodes  $\mathbf{C}_w$ " as shown in Figs.7 (b) and (d).

### 3.3 WG discretization

The high-order B-spline scaling/wavelet functions do not have the so-called Kronecker-delta property as shown in Figs.1 (a) and (b). A penalty formulation is employed to impose essential boundary conditions. The virtual work principle including the penalty term is written, as:

$$\int_{\Omega} \boldsymbol{\epsilon}(\delta \mathbf{u}^{xw}) : \mathbf{D} : \boldsymbol{\epsilon}(\mathbf{u}^{xw}) d\Omega + \alpha \int_{\Gamma_u} \delta \mathbf{u}^{xw} \cdot (\mathbf{u}^{xw} - \bar{\mathbf{u}}) d\Gamma_u = \int_{\Gamma_t} \delta \mathbf{u}^{xw} \cdot \bar{\mathbf{t}} d\Gamma_t, \quad (8)$$

where  $\mathbf{u}^{xw}$  is the displacement vector of the XWGM presented in eq. (5), and  $\delta \mathbf{u}^{xw}$  is the variation.  $\boldsymbol{\epsilon}(\mathbf{u}^{xw})$  denotes the strain components and  $\boldsymbol{\epsilon}(\delta \mathbf{u}^{xw})$  the variation.  $\bar{\mathbf{u}}$  and  $\bar{\mathbf{t}}$  are the displacement and traction vectors prescribed on  $\Gamma_u$  and  $\Gamma_t$ , respectively.  $\alpha$  is a large positive number that imposes the essential boundary conditions.  $\mathbf{D}$  is an elastic constant matrix.

The weak form in eq. (8) is discretized employing the XWGM. The level- $(l+1)$  displacements  $\mathbf{u}_{l+1}^{xw}(\mathbf{x})$  are represented in matrix form as

$$\mathbf{u}_{l+1}^{xw}(\mathbf{x}) = \mathbf{N}_{l+1} \mathbf{U}_{l+1}^{xw}, \quad (9)$$

where the matrix  $\mathbf{N}_{l+1}$  is composed of the scaling/wavelet functions including the enrichment terms. The vector  $\mathbf{U}_{l+1}^{xw}$  is the coefficient vector. The matrix  $\mathbf{N}_{l+1}$  and the coefficient vectors  $\mathbf{U}_{l+1}^{xw}$  are written as

$$\mathbf{N}_{l+1} = [\boldsymbol{\Phi}_l \boldsymbol{\Psi}_l^1 \boldsymbol{\Psi}_l^2 \boldsymbol{\Psi}_l^3 \boldsymbol{\Phi}_l^{J_s} \boldsymbol{\Phi}_l^{C_s} \boldsymbol{\Psi}_l^{1, C_w} \boldsymbol{\Psi}_l^{2, C_w} \boldsymbol{\Psi}_l^{3, C_w}], \quad (10)$$

$$\mathbf{U}_{l+1}^{xw} = (\mathbf{a}_l \mathbf{b}_l^1 \mathbf{b}_l^2 \mathbf{b}_l^3 \mathbf{c}_l \mathbf{d}_l \mathbf{e}_l^1 \mathbf{e}_l^2 \mathbf{e}_l^3)^T, \quad (11)$$

where  $\boldsymbol{\Phi}_l$  and  $\boldsymbol{\Psi}_l^m(m = 1, 2, 3)$  are components represented by the 2D level- $l$  scaling/wavelet functions.  $\boldsymbol{\Phi}_l^{J_s}(= H(\mathbf{x})\boldsymbol{\Phi}_l)$  is a component that represents the displacement discontinuity of the crack face in terms of the nodes  $\mathbf{J}_s$ . In addition,  $\boldsymbol{\Phi}_l^{C_s}$  and  $\boldsymbol{\Psi}_l^{m, C_w}$  are coupling terms of the enrichment functions regarding the nodes  $\mathbf{C}_s$  and  $\mathbf{C}_w$ , respectively. The matrix components  $\boldsymbol{\Phi}_l^{C_s}$  and  $\boldsymbol{\Psi}_l^{m, C_w}$  can be written as

$$\boldsymbol{\Phi}_l^{C_s} = [\gamma_1(\mathbf{x})\boldsymbol{\Phi}_l \gamma_2(\mathbf{x})\boldsymbol{\Phi}_l \gamma_3(\mathbf{x})\boldsymbol{\Phi}_l \gamma_4(\mathbf{x})\boldsymbol{\Phi}_l], \quad (12)$$

$$\boldsymbol{\Psi}_l^{m, C_w} = [\gamma_1(\mathbf{x})\boldsymbol{\Psi}_l^m \gamma_2(\mathbf{x})\boldsymbol{\Psi}_l^m \gamma_3(\mathbf{x})\boldsymbol{\Psi}_l^m \gamma_4(\mathbf{x})\boldsymbol{\Psi}_l^m], (m = 1, 2, 3), \quad (13)$$

where  $\mathbf{a}_l$  and  $\mathbf{b}_l^m$  are coefficient vectors for the level- $l$  scaling/wavelet functions.  $\mathbf{c}_l$  is the coefficient vector of the nodes  $\mathbf{J}_s$ .  $\mathbf{d}_l$  and  $\mathbf{e}_l^m$  are coefficients belonging to the nodes  $\mathbf{C}_s$  and  $\mathbf{C}_w$ , respectively.

Substituting the level- $(l+1)$  displacement  $\mathbf{u}_{l+1}^{xw}(\mathbf{x})$  into the virtual work of principle of eq. (8), the linear simultaneous equation

$$(\mathbf{K}_{l+1} + \mathbf{K}_{l+1}^\alpha) \mathbf{U}_{l+1}^{xw} = \mathbf{f}_{l+1} + \mathbf{f}_{l+1}^\alpha \quad (14)$$

is obtained, where  $\mathbf{K}_{l+1}$  is a stiffness matrix and  $\mathbf{f}_{l+1}$  is an external force vector.  $\mathbf{K}_{l+1}^\alpha$  and  $\mathbf{f}_{l+1}^\alpha$  are the matrix and vector for the penalty term. They can be written using the matrix  $\mathbf{N}_{l+1}$  as

$$\mathbf{K}_{l+1} = \int_{\Omega} \mathbf{B}_{l+1}^T \mathbf{D} \mathbf{B}_{l+1} d\Omega, \quad \mathbf{f}_{l+1} = \int_{\Gamma_t} \mathbf{N}_{l+1}^T \bar{\mathbf{t}} d\Gamma_t, \quad (15)$$

$$\mathbf{K}_{l+1}^\alpha = \int_{\Gamma_u} \mathbf{N}_{l+1}^T \mathbf{N}_{l+1} d\Gamma_u, \quad \mathbf{f}_{l+1}^\alpha = \int_{\Gamma_u} \mathbf{N}_{l+1}^T \bar{\mathbf{u}} d\Gamma_u, \quad (16)$$

where  $\mathbf{B}_{l+1}$  is the displacement gradient matrix.

Gauss quadrature is chosen to numerically integrate the stiffness matrix. In the standard WGM without the enrichment functions,  $3 \times 3$  and  $4 \times 4$  Gauss integrations are adopted for quadratic and cubic B-splines based on the level- $l$ ,  $-(l+1)$ ,  $-(l+2)$ ,  $\dots$  cells. For the stiffness matrix including the enrichment functions of nodes  $\mathbf{C}_s$ ,  $\mathbf{C}_w$  and  $\mathbf{J}_s$  in the XWGM, the cells are divided into  $ndiv \times ndiv$  sub-cells for the numerical integration as shown in Fig.7 (d). The number of divisions was examined in [29] for the linear B-spline case and the numerical solutions almost converged with  $ndiv = 4$  or 8; we employ the same divisions in the high-order B-spline cases.

### 3.4 Calculation of SIFs for 2D crack problems

The  $J$ -integral [36] is adopted to evaluate the SIFs and thus examine the accuracy of the 2D fracture mechanics analysis. A schematic illustration of the path-independent integral is shown in Fig.8 (a). The  $J$ -integral is written, as:

$$J = \int_{\Gamma} (W dx'_2 - t_i \frac{\partial u_j}{\partial x'_1}) d\Gamma, \quad (17)$$

where  $\Gamma$  is a curve surrounding the crack tip and  $W (= \sigma_{ij} \epsilon_{ij})$  is the strain energy density.  $t_i (= n_j \sigma_{ji})$  is the traction vector,  $u_i$  is the displacement vector, and  $n_i$  is the unit vector normal to  $\Gamma$ .  $x'_1$  and  $x'_2$  are the directions along and normal to the crack line, respectively.

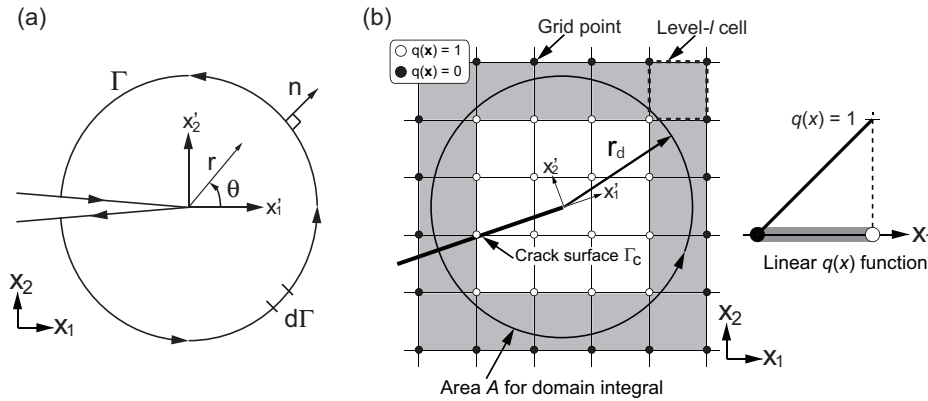


**Fig. 8**  $J$ -integral and the EDI: **a**  $J$ -integral, **b** Discretization of EDI in the XWGM

For the convenience of numerical implementation, the equivalent domain integral (EDI) form is adopted. The  $J$ -integral of the EDI form is written as

$$J = - \int_A (W \delta_{1i} - \sigma_{ij} \frac{\partial u_j}{\partial x'_1}) \frac{q(\mathbf{x})}{\partial x'_i} dA, \quad (18)$$

where  $A$  is area for the EDI. In the EDI form, a continuous and smooth function  $q(\mathbf{x})$  is needed. In the XWGM, a plateau-type function is adopted employing the lowest-resolution cells (level- $l$  cell) as shown in Fig.8. When the grid points are within the radius  $r_d$  from the crack tip,  $q(\mathbf{x})=1$ ; otherwise,  $q(\mathbf{x})=0$ . Mixed-mode crack problems are next treated in numerical examples. To separate the  $J$  value into mode  $K_I$  and  $K_{II}$  components, an interaction integral is adopted. The details of the interaction integral are presented in [27,28].

## 4 Numerical examples

Several 2D crack problems are solved employing the XWGM. Convergence studies are carried out to examine the accuracy of the fracture mechanics analysis employing the quadratic and cubic B-spline scaling/wavelet functions. Furthermore, 2D fracture test specimens are analyzed to verify the effectiveness of the fixed-grid approach. Two kinds of the enrichment techniques are examined. One employs (A) nodes  $\mathbf{J}_s$  and  $\mathbf{C}_s$  (a scaling function only) and the other employs (B) nodes  $\mathbf{J}_s$ ,  $\mathbf{C}_s$  and  $\mathbf{C}_w$  (a scaling function and the multilevel wavelet functions). The results of the XWGM for the linear B-spline case are also presented to examine the numerical results. Poisson's ratio is  $\nu = 0.3$ , and a plane stress condition is assumed in the numerical examples.

### 4.1 Edge crack problem under uniform tension

A problem of a rectangular plate with an edge crack is solved. The dimensions of the plate are width  $W = 10.0$  (mm) and height  $H = 10.0$  (mm) as shown in Fig.9 (a). The length of the edge crack is  $a = 5.0$  (mm). Uniform tensile stress  $\sigma_{22} = 1.0$  (MPa) is applied to the top and bottom of the plate. The division for numerical integration of the stiffness matrix is chosen  $ndiv = 8$ .

The enrichment technique (A) is first examined. The rectangular plate is divided by  $15 \times 15$  equally spaced structured cells (level- $l$  cells), and the XWG model is assumed to be the level- $l$  model as shown in Fig.9 (b). Level- $l$  scaling functions are periodically located on the model. The node arrangements of the quadratic and cubic B-spline scaling functions are respectively shown in Figs.9 (c) and (d). The function support of the level- $l$  scaling functions is presented in the figures. Because the high-order B-spline scaling functions span a number of cells, the nodes located in the external domain are needed to construct the stiffness matrix. Three kinds of the uniform refinement models (*i.e.*, the rectangular plate is divided by  $31 \times 31$ ,  $63 \times 63$  and  $127 \times 127$  structured cells) are also analyzed to carry out the convergence study. As the spatial resolution increases in the uniform refinement models, the density of the nodes uniformly increases. The scaling functions in terms of the cell at the crack tip are only assigned nodes  $\mathbf{C}_s$  as shown in Figs.9 (c) and (d). The other scaling functions in terms of the cells across the crack segment are assigned nodes  $\mathbf{J}_s$  in the XWG models. SIF  $K_I$  is evaluated using the EDI form of the  $J$ -integral in eq. (18). The radius for the EDI is chosen as  $r_d = 5.0$  (mm). The error in the SIF is evaluated according to

$$error = \frac{|K^{Num} - K^{Ref}|}{K^{Ref}} \times 100(\%), \quad (19)$$

where  $K^{Num}$  is the evaluated SIF. Additionally,  $K^{Ref}$  is the reference solution. In this case,  $K^{Ref} = 11.93$  (MPa mm<sup>1/2</sup>) [37] is used.

To examine the effects of number of the enrichment functions  $\gamma_n(\mathbf{x})$  ( $n = 1, \dots, n_e$ ) at nodes  $\mathbf{C}_s$ , XWG analyses are carried out with  $n_e = 1$  and 4. The numerical results in the case  $n_e = 1$  for the quadratic and cubic B-spline scaling functions are presented in Table 1. The results obtained with the linear B-spline scaling functions are also presented. As the DOFs increase, the error in the SIF uniformly converges in all cases. The inclination of the convergence is better when higher-order B-splines are adopted. The results for the case  $n_e = 4$  are shown in Table 2. The results are more accurate than the results of the case  $n_e = 1$ . When the quadratic and cubic B-splines are adopted in the XWG analysis, the errors in the SIFs are less than 1% even in the level- $l$  model. It is found that

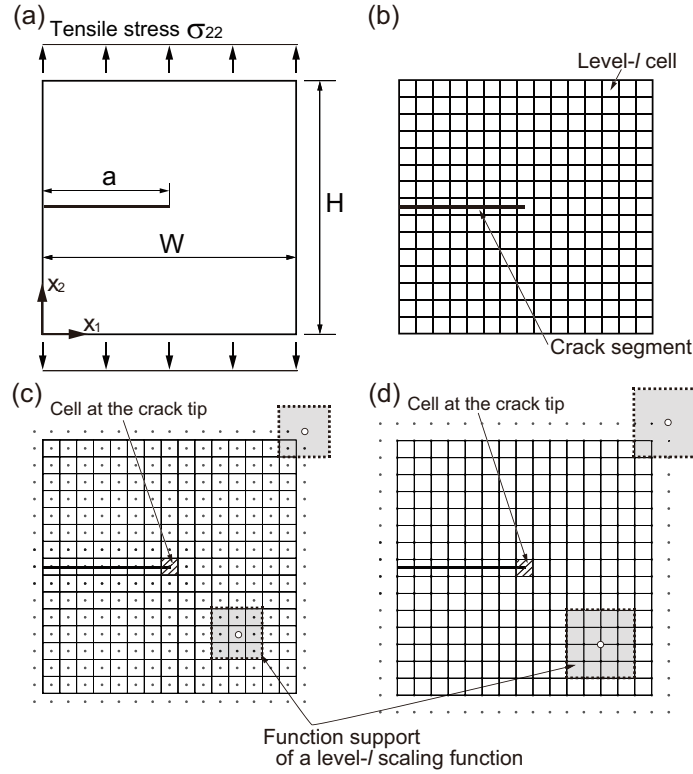


**Fig. 9** Edge crack problem under uniform tension: **a** Analysis model to be solved, **b**  $15 \times 15$  equally spaced structured cells, **c** Level- $l$  model (Quadratic B-spline), **d** Level- $l$  model (Cubic B-spline)

**Table 1** Crack analysis with the high-order B-spline scaling functions (Enrichment technique (A);  $n_e = 1$ )

	Quadratic		Cubic		Linear	
	DOF	error(%)	DOF	error(%)	DOF	error(%)
15 div.	638	3.280	736	1.565	548	5.614
31 div.	2,286	1.571	2,464	0.791	2,116	2.613
63 div.	8,654	0.785	8,992	0.410	8,324	1.272
127 div.	33,678	0.409	34,336	0.225	33,028	0.644

**Table 2** Crack analysis with the high-order B-spline scaling functions (Enrichment technique (B);  $n_e = 4$ )

	Quadratic		Cubic		Linear	
	DOF	error(%)	DOF	error(%)	DOF	error(%)
15 div.	692	0.345	832	0.060	572	3.512
31 div.	2,340	0.185	2,560	0.057	2,140	1.534
63 div.	8,708	0.112	9,088	0.049	8,348	0.726
127 div.	33,732	0.077	34,432	0.047	33,052	0.370

the displacements and the stress distributions near the crack tip can be represented with fewer DOFs in the fixed-grid approach. Additionally, the accuracy is improved when the high-order B-spline scaling functions are employed in the XWG analysis.

Enrichment technique (B) is now examined. Because high accuracy results are obtained when  $n_e = 4$  is chosen in enrichment technique (A), convergence studies are carried out for the case  $n_e = 1$  after the numerical examples to examine the effectiveness of the multilevel wavelet bases. The level- $l$  models of Figs.9 (c) and (d) are employed as the lowest resolution models for the XWG analyses with the quadratic and cubic B-splines. The level- $l$ ,  $-(l+1)$  and  $-(l+2)$  wavelet functions are superposed on the

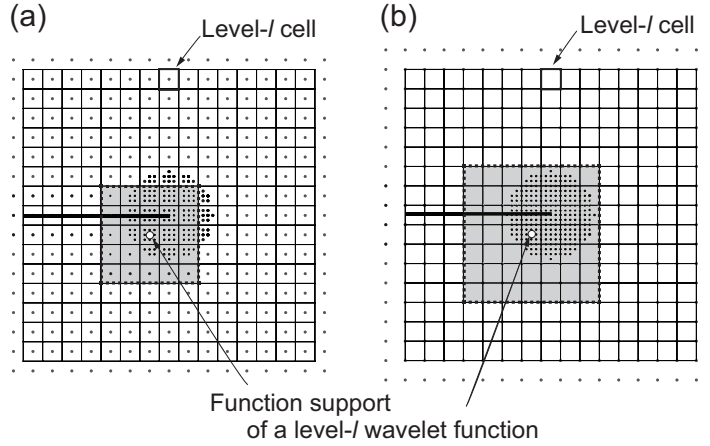


**Fig. 10** Crack analysis with the high-order B-spline scaling/wavelet functions ( $r_e=1.5$  (mm)): **a** Level- $(l+2)$  model (Quadratic B-spline), **b** Level- $(l+2)$  model (Cubic B-spline)

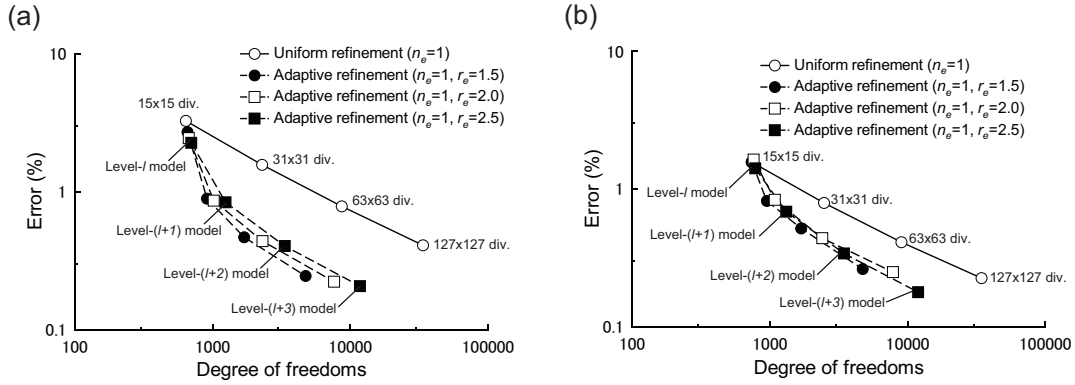


**Fig. 11** Convergence studies for edge crack problem under tension with the different resolution models: **a** Quadratic B-spline, **b** Cubic B-spline

level- $l$  model to refine the solutions around the crack tip. The models are called the adaptive refinement models. The level- $(l+2)$  models for the quadratic and cubic B-splines are respectively shown in Figs.10 (a) and (b). A function support of the level- $l$  quadratic and cubic wavelet functions are also presented in the figures. In the XWG models presented in Figs.10 (a) and (b), the level- $l$  scaling functions and the level- $l$  and  $-(l+1)$  wavelet functions within a radius  $r_e = 1.5$  (mm) of the crack tip are assigned enriched nodes  $\mathbf{C}_s$  and  $\mathbf{C}_w$ . Furthermore, the other level- $l$  scaling functions in terms of the cells crossing the crack segment are assigned enriched nodes  $\mathbf{J}_s$ .

The errors in  $K_I$  of the XWG models with the quadratic and cubic B-splines are presented in Figs.11 (a) and (b). The horizontal axis represents the DOFs of the XWG analyses. The solid lines represent the results of uniform refinement models of case (A) employing the  $15 \times 15$ ,  $31 \times 31$ ,  $63 \times 63$  and  $127 \times 127$  structured cells presented in Table 1. The dashed lines are the results for the adaptive refinement models when  $r_e = 1.5, 2.0, 2.5$  (mm) are employed with the level- $l$ ,  $-(l+1)$ ,  $-(l+2)$  and  $-(l+3)$  models. The results of the solid lines (uniform refinement models) can be considered as an X-FEM model with equally spaced quadrilateral elements (voxel-based X-FEM). Because the multilevel wavelet functions are added around the crack tip, the XWGM is then carried out the crack analyses with fewer DOFs compared with the voxel-based X-FEM. Therefore, effective fracture mechanics can be carried out employing the present method. Although the wavelet functions at the nodes  $\mathbf{C}_w$  do not satisfy the PU condition, error in the SIFs converges. Additionally, the convergence is better than that for uniform refinement results. Therefore, highly accurate results are obtained with fewer DOFs

employing the multilevel wavelet bases in the XWGM.

#### 4.2 Circular plate with an inclined crack subjected to a compression load

The problem of a circular plate test specimen with an inclined crack is solved. The model is shown in Fig.12 (a). This is the so-called Brazilian disk test and the problem was solved in [38]. The radius of the plate is  $R=5.0$  (mm). Compressive forces  $P=1.0$  (KN) are enforced on both sides of the cracked specimen. The SIFs  $K_I$  and  $K_{II}$  are evaluated varying the crack length  $2a$  and the angle of inclination  $\theta$ . In the XWGM, it is easy to model such curved surfaces because the discretization is based on a fixed-grid. The sub-cell approach is effective in modeling the external boundaries in the XWGM.

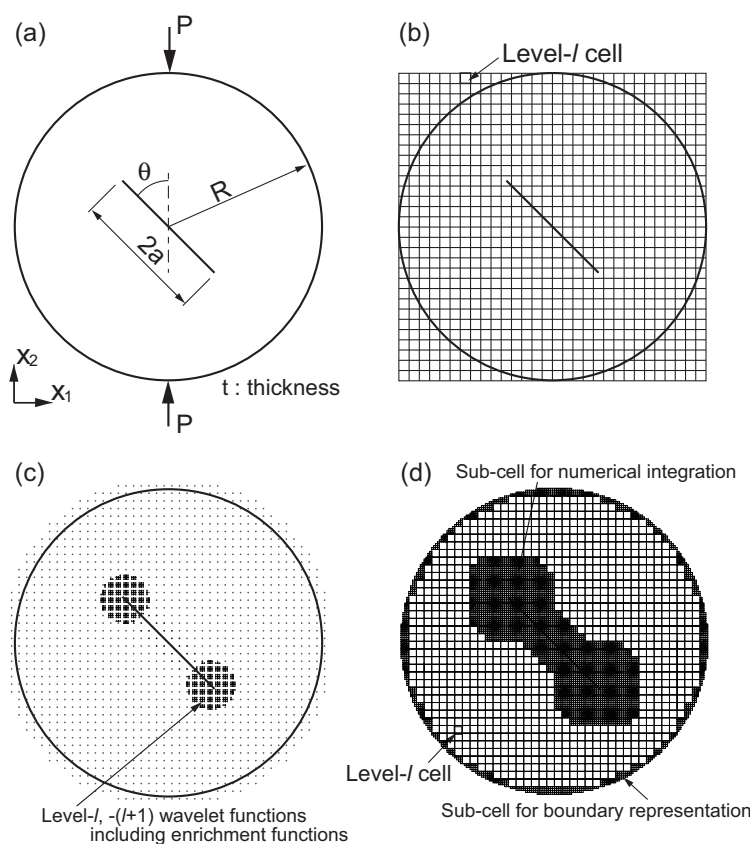


**Fig. 12** Circular plate with an inclined crack: **a** Analysis model to be solved, **b**  $30 \times 30$  equally spaced structured cells (Level- $l$  cells), **c** Level- $(l+2)$  model (Quadratic B-spline), **d** Cells and sub-cells in the XWG model

The cracked circular plate is covered by  $30 \times 30$  equally spaced structured cells (level- $l$  cells) as shown in Fig.12 (b). The level- $l$  model is generated based on the level- $l$  cells. The level- $(l+2)$  models are employed in the XWG analyses by superposing the level- $l$  and  $-(l+1)$  wavelet functions on the level- $l$  models. The inclined crack is modeled by introducing the enrichment functions  $C_s$ ,  $C_w$  and  $J_s$  to the level- $(l+2)$  models. The radius of the enrichments  $r_e=0.8$  (mm), and the radius for the EDI is  $r_d=1.5$  (mm). The division for the numerical integration is  $ndiv=4$ . For example, the level- $(l+2)$  model with the quadratic B-splines is schematically illustrated in Fig.12 (c). The level- $l$ , and  $-(l+1)$  wavelet functions including the enrichment functions  $C_s$  and  $C_w$  are located near the crack tip. Furthermore, the cells and sub-cells of the numerical integration of the stiffness matrix in the level- $(l+2)$  model are presented in Fig.12 (d). The sub-cells located at the external boundary are used to represent the

boundaries. The sub-cells located within the analysis domain are employed to accurately integrate the stiffness matrix including the enrichment functions.

The SIFs  $K_I$  and  $K_{II}$  are normalized as

$$K_I = F_I \frac{P\sqrt{\pi a}}{\pi R t}, \quad K_{II} = F_{II} \frac{P\sqrt{\pi a}}{\pi R t}, \quad (20)$$

where  $F_I$  and  $F_{II}$  are normalized SIFs, and  $t$  is the plate thickness.  $F_I$  and  $F_{II}$  are evaluated for crack lengths  $a/R = 0.3, 0.4$  and  $0.5$  while varying the angles of inclination  $\theta = \pi/16 \times i$  ( $i = 0, 2, 4, 6, 8$ ). The results for  $a/R = 0.3, 0.4$  and  $0.5$  are presented in Tables 3, 4 and 5. The SIFs  $F_I^\mu$  and  $F_{II}^\mu$  correspond to the SIFs with quadratic ( $\mu = 3$ ) and cubic ( $\mu = 4$ ) B-spline scaling/wavelet functions.  $F_I^{Ref}$  and  $F_{II}^{Ref}$  are the reference solutions in [38]. In all cases, the results are in good agreement with the reference solutions. It is thus found that the 2D crack problems including curved surfaces are easy to solve employing XWG analyses and the sub-cell approach.

**Table 3** Comparison with normalized SIFs  $F_I$  and  $F_{II}$  ( $a/R=0.3$ )

$i$	$F_I^3$	$F_I^4$	$F_I^{Ref}$	$F_{II}^3$	$F_{II}^4$	$F_{II}^{Ref}$
0	1.134	1.133	1.136	0.000	0.000	0.000
2	0.321	0.320	0.320	1.661	1.662	1.662
4	-1.302	-1.305	-1.306	2.066	2.069	2.069
6	-2.593	-2.592	-2.596	1.310	1.312	1.311
8	-3.053	-3.052	-3.056	0.000	0.000	0.000

**Table 4** Comparison with normalized SIFs  $F_I$  and  $F_{II}$  ( $a/R=0.4$ )

$i$	$F_I^3$	$F_I^4$	$F_I^{Ref}$	$F_{II}^3$	$F_{II}^4$	$F_{II}^{Ref}$
0	1.241	1.241	1.243	0.000	0.000	0.000
2	0.215	0.214	0.214	1.864	1.853	1.859
4	-1.525	-1.528	-1.528	2.096	2.101	2.100
6	-2.716	-2.719	-2.723	1.256	1.242	1.249
8	-3.115	-3.114	-3.115	0.000	0.000	0.000

**Table 5** Comparison with normalized SIFs  $F_I$  and  $F_{II}$  ( $a/R=0.5$ )

$i$	$F_I^3$	$F_I^4$	$F_I^{Ref}$	$F_{II}^3$	$F_{II}^4$	$F_{II}^{Ref}$
0	1.385	1.385	1.387	0.000	0.000	0.000
2	0.036	0.037	0.030	2.123	2.119	2.113
4	-1.790	-1.793	-1.784	2.122	2.124	2.132
6	-2.868	-2.867	-2.885	1.206	1.195	1.188
8	-3.216	-3.215	-3.208	0.000	0.000	0.000

#### 4.3 Cruciform test specimen including an inclined crack

A cruciform test specimen including an inclined crack is solved to further validate the XWGM. The test specimen was analyzed in [39, 40]. The model configuration is presented in Fig.13 (a). The dimensions of the specimen are  $2H=150$  (mm),  $2W=100$  (mm),  $2L=200$  (mm) and  $2S=330$  (mm). Tensile stress

$\sigma_{22}=1.0$  (MPa) is applied to the top and bottom surfaces of the model. An inclined crack is introduced to the center of the specimen, and the mixed mode SIFs  $K_I$  and  $K_{II}$  are evaluated while varying the crack length  $2a$  and the angle of inclination  $\theta$ .

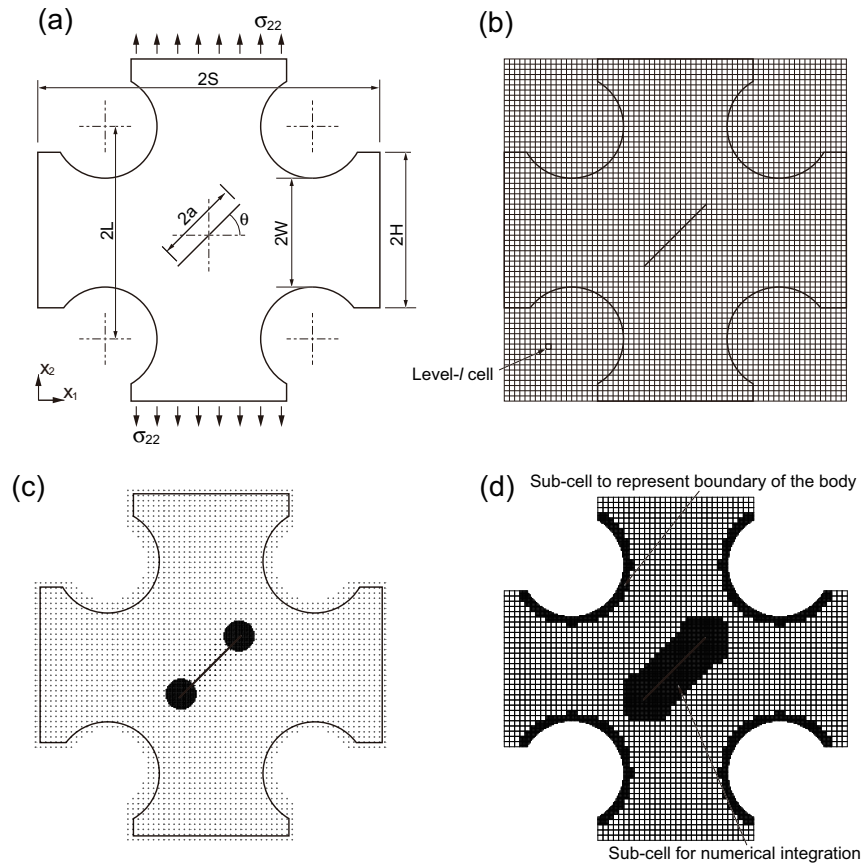


**Fig. 13** Cruciform test specimen including an inclined crack: **a** Analysis model to be solved, **b**  $66 \times 66$  equally spaced structured cells (Level- $l$  cell), **c** Level- $(l+2)$  model (Cubic B-spline), **d** Cells and sub-cells in the XWG model

The test specimen is covered by  $66 \times 66$  structured cells (level- $l$  cells) as shown in Fig.13 (b). The dimensions of the unit cell are  $5.0 \times 5.0$  (mm), and the level- $l$  model is generated using a fixed-grid. The level- $(l+2)$  models are employed. The radius for the enrichment functions  $C_s$  and  $C_w$  is  $r_e = 15.0$  (mm). The division for the numerical integration is  $ndiv = 4$ . The radius for the EDI is  $r_e = 30.0$  (mm). The node arrangements of the XWG model with the cubic B-splines are presented in Fig.13(c). The locations of the cells and sub-cells of the level- $(l+2)$  model are presented in Fig.13(d). The sub-cell approach is adopted to represent the external boundary of the model, and to employ the numerical integration of the stiffness matrix including the enrichment functions. The normalized SIFs  $F_I = K_I/\sqrt{\pi a}$  and  $F_{II} = K_{II}/\sqrt{\pi a}$  are evaluated while varying the crack angle  $\theta = \pi/12 \times i$  ( $i = 0, 1, 2, 3, 4, 5, 6$ ) for crack lengths of  $a/W = 0.6, 0.8$  and  $1.0$ .

The SIFs are also evaluated using the FEM for comparison. Commercial FEM software MSC.Marc [41] is adopted. The crack option is set to calculate the mixed mode SIFs. The FEM model is presented in Fig.14 (a), and a close-up view near the crack is shown in Fig.14 (b). Quadratic triangle/quadrilateral elements are employed. The whole structure is modeled with  $5.0 \times 5.0$  (mm) elements, and  $1.0 \times 1.0$  (mm) elements are employed near the crack. The total numbers of nodes and elements of the FEM model presented in Fig.14 (a) are 16,540 and 5,632, respectively. FEM modeling of a structure with general boundaries including cracks is sometimes cumbersome because very small elements are needed

to represent severe stress concentration near the crack tip, and double nodes are needed along the crack segment to represent the displacement discontinuity. However, the XWGM can reduce such modeling tasks by introducing enrichment functions in the fixed-grid approach.

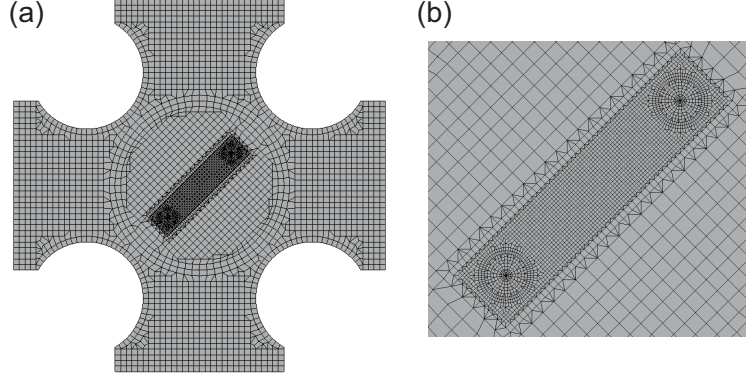


**Fig. 14** FEM model of the cruciform test specimen: **a** FEM model, **b** Close-up view

The  $F_I$  of the XWGM computations is compared with the FEMs and the reference solutions. The reference solutions  $F_I^{Ref}$  for various  $a/W$  are evaluated by following equation [39, 40], as:

$$F_I^{Ref} = 1.1906 + 0.0076 \times \frac{a}{W} + 0.2051 \times \left(\frac{a}{W}\right)^2 - 0.0042 \times \left(\frac{a}{W}\right)^3, \quad 0.2 \leq a/W \leq 1.0. \quad (21)$$

The results are shown in Table 6.  $F_I^3$  and  $F_I^4$  are normalized SIF  $F_I$  obtained the XWGM with quadratic and cubic B-splines. The differences in the SIFs are less than 1 %. In addition, the mixed mode SIFs  $F_I$  and  $F_{II}$  obtained with the XWGM are compared with those of the FEM results for several angles  $\theta$ . The results are presented in Figs.15 (a) and (b) for  $F_I$  and  $F_{II}$ , respectively. The results are in good agreements for all crack angles  $\theta$ .

**Table 6** Comparison of normalized SIF  $F_I$  ( $a/W = 0.6, 0.8, 1.0, \theta = 0$ )

$a/W$	$F_I^3$	$F_I^4$	$F_I^{FEM}$	$F_I^{Ref}$
0.6	1.266	1.267	1.267	1.268
0.8	1.325	1.325	1.325	1.326
1.0	1.398	1.398	1.398	1.399

## 5 Conclusion

2D fracture mechanics analyses are carried out employing the XWGM. Enrichment functions of the X-FEM are introduced in the crack modeling in the WGM with high-order B-spline scaling/wavelet functions. It is confirmed that 2D fracture mechanics analysis can be carried out employing the WGM with high-order B-splines by introducing the enrichment functions to represent displacement discontinuity and severe stress concentration near the crack tip. Furthermore, highly accurate computations are made and fracture mechanics parameters are evaluated using the high-order B-spline wavelet bases instead of linear B-spline scaling functions. Because the WGM is a fixed-grid approach, it is easy to make an analysis model with curved boundaries. In addition, by introducing the enrichment functions, fracture mechanics analysis is easily conducted employing the XWGM.

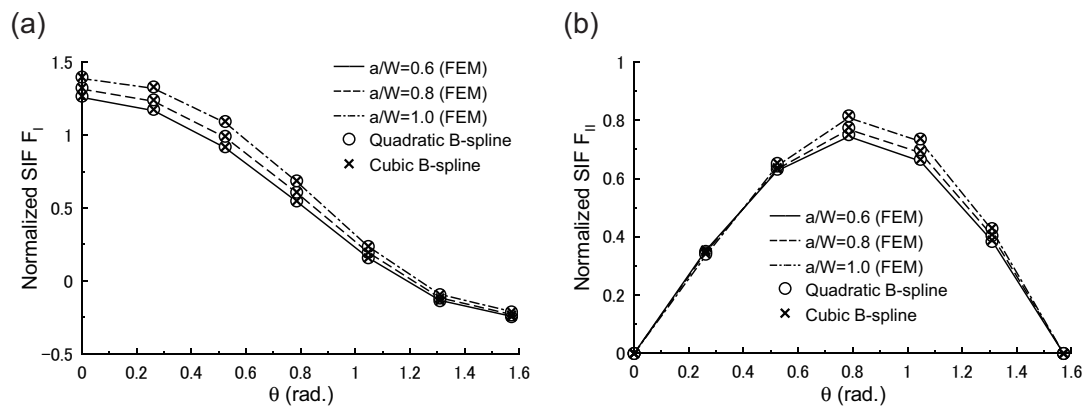


Fig. 15 Comparison of normalized SIFs: **a**  $F_I$ , **b**  $F_{II}$

## Acknowledgements

This research was partially supported by the Grant for Young Researchers from the JGC-S Scholarship Foundation.

## References

1. Daubechies, I.: Ten lectures on wavelets. SIAM, Philadelphia (1992)
2. Mayer, Y.: Wavelets: algorithms and applications. SIAM, Philadelphia (1993)
3. Chui, C.K.: Wavelets: a mathematical tool for signal analysis. SIAM, Philadelphia (1997)
4. Amaratunga, K., Williams, J.R.: Wavelet based Green's function approach to 2D PDEs. Eng. Computation. **10**, 349-367 (1993)
5. Williams, J.R., Amaratunga, K.: Introduction to wavelets in engineering. Int. J. Numer. Meth. Eng. **37**, 2365-2388 (1994)
6. Amaratunga, K., Williams, J.R., Qian, S., Weiss, J.: Wavelet-Galerkin solutions for one-dimensional partial differential equations. Int. J. Numer. Meth. Eng. **37**, 2703-2716 (1994)
7. Bertoluzza, S., Naldi, G.: A wavelet collocation method for the numerical solution of partial differential equations. Appl. Comput. Harm. Anal. **3**, 1-9 (1996)
8. Lu, D., Ohyoshi, T., Miura, K.: Treatment of boundary conditions in one-dimensional wavelet-Galerkin method. JSME International Journal. Ser. A. **40**, 382-388 (1997)
9. Diaz, A.R.: A wavelet-Galerkin scheme for analysis of large-scale problems on simple domains. Int. J. Numer. Meth. Eng. **44**, 1599-1616 (1999)
10. Chen, W.-H., Wu, C.-W.: A spline wavelets element method for frame structures vibration. Comput. Mech. **16**, 11-21 (1995)
11. Kurdila, A.J., Sun, T., Grama, P., Ko, J.: Affine fractal interpolation functions and wavelet-based finite elements. Comput. Mech. **17**, 169-185 (1995)
12. Koro, K., Abe, K.: Non-orthogonal spline wavelets for boundary element analysis. Eng. Anal. Bound. Elem. **25**, 149-164 (2001)
13. Koro, K., Abe, K.: A practical determination strategy of optimal threshold parameter for matrix compression in wavelet BEM. Int. J. Numer. Meth. Eng. **57**, 169-191 (2003)
14. Li, B., Chen, X.: Wavelet-based numerical analysis: A review and classification. Finite. Elem. Anal. Des. **81**, 14-31 (2014)
15. Hollister, S.J., Kikuchi, N.: Homogenization theory and digital imaging: A basis for studying the mechanics and design principles of bone tissue. Biotechnol. Bioeng. **43**, 586-596 (1994)
16. Terada, K., Miura, T., Kikuchi, N.: Digital image-based modeling applied to the homogenization analysis of composite materials. Comput. Mech. **20**, 331-346 (1997)
17. Nakagoshi, S., Noguchi, H.: A modified wavelet Galerkin method for analysis of Mindlin plates. JSME International Journal. Ser. A. **44**, 610-615 (2001)
18. Zhang, L., Wang, J., Zhou, Y.-H.: Wavelet solution for large deflection bending problems of thin rectangular plates. Arch. Appl. Mech. 10.1007/s00419-014-0960-9 (2014)
19. Comincioli, V., Scapolla, T., Naldi, G., Venini, P.: A wavelet-like Galerkin method for numerical solution of variational inequalities arising in elastoplasticity. Comm. Numer. Meth. Eng. **16**, 133-144 (2000)
20. Venini, P., Morana, P.: An adaptive wavelet-Galerkin method for an elastic-plastic-damage constitutive model: 1D problem. Comput. Meth. Appl. Mech. Eng. **190**, 5619-5638 (2001)
21. Jang, G.W., Kim, J.E., Kim, Y.Y.: Multiscale Galerkin method using interpolation wavelets for two-dimensional elliptic problems in general domains. Int. J. Numer. Meth. Eng. **59**, 225-253 (2004)

- 
22. DeRose Jr., G.C.A., Diaz, A.R.: Solving three-dimensional layout optimization problems using fixed scale wavelets. *Comput. Mech.* **25**, 274-285 (2000)
  23. Poulsen, T.A.: Topology optimization in wavelet space. *Int. J. Numer. Meth. Eng.* **53**, 567-582 (2002)
  24. Kim, J.E., Jang, G.W., Kim, Y.Y.: Adaptive multiscale wavelet-Galerkin analysis for plane elasticity problems and its application to multiscale topology design optimization. *Int. J. Solid. Struct.* **40**, 6473-6496 (2003)
  25. Tanaka, S., Okada, H., Okazawa, S.: A wavelet Galerkin method employing B-spline bases for solid mechanics problems without the use of fictitious domain. *Comput. Mech.* **50**, 35-48 (2012)
  26. Chui, C.K., Wang, J.Z.: A cardinal spline approach to wavelets. *Proc. Am. Math. Soc.* **113**, 785-793 (1991)
  27. Belytschko, T., Black, T.: Elastic crack growth in finite elements with minimal remeshing. *Int. J. Numer. Meth. Eng.* **45**, 601-620 (1999)
  28. Moës, N., Dolbow, J., Belytschko, T.: A finite element method for crack growth without remeshing. *Int. J. Numer. Meth. Eng.* **46**, 131-150 (1999)
  29. Tanaka, S., Okada, H., Okazawa, S., Fujikubo, M.: Fracture mechanics analysis using the wavelet Galerkin method and extended finite element method. *Int. J. Numer. Meth. Eng.* **93**, 1082-1108 (2013)
  30. Li, S., Ghosh, S.: Extended Voronoi cell finite element model for multiple cohesive crack propagation in brittle materials. *Int. J. Numer. Meth. Eng.* **65**, 1028-1067 (2006)
  31. Li, S., Ghosh, S.: Multiple cohesive crack growth in brittle materials by the extended Voronoi cell finite element model. *Int. J. Fract.* **141**, 373-393 (2006)
  32. Menouillard, T., Belytschko, T.: Dynamic fracture with meshfree enriched X-FEM. *Acta Mech.* **213**, 53-69 (2010)
  33. Liu, Z.L., Menouillard, T., Belytschko, T.: An XFEM/Spectral element method for dynamic crack propagation. *Int. J. Fract.* **169**, 183-198 (2011)
  34. Christon, M.A., Roach, D.W.: The numerical performance of wavelets for PDEs: the multi-scale finite element. *Comput. Mech.* **25**, 230-244 (2000)
  35. Melenk, J.M., Babuška, I.: The partition of unity finite element method: Basic theory and applications. *Comput. Mech.* **139**, 289-314 (1996)
  36. Rice, J.R.: A path independent integral and the approximate analysis of strain concentration by notches and cracks. *J. Appl. Mech.* **35**, 379-386 (1968)
  37. Bowe, O.L.: Solutions of plane crack problems by mapping technique (Chapter 1), *Mechanics of fracture* (edited by Sih G.C.), 1-55, Noordhoff, International Publishing, Leyden, The Netherlands (1972)
  38. Atkinson, C., Smelser, R.E., Sanchez, J.: Combined mode fracture via the cracked Brazilian disk test. *Int. J. Fract.* **18**, 279-291 (1982)
  39. Kitagawa, H., Yuuki, R., Tohgo, K.: Fatigue crack growth characteristics of mixed mode cracks. *Trans. Jpn. Soc. Mech. Eng.* **47**, 1283-1292 (1981) (in Japanese)
  40. Kitagawa, H., Yuuki, R.: A fracture mechanics approach to high-cycle fatigue crack growth under in-plane biaxial loads. *Fatig. Fract. Eng. Mater. Struct.* **2**, 195-206 (1979) (in Japanese)
  41. MSC.Marc 2005r3, User's Guide